

# Graphene Oxide Flakes Tune Excitatory Neurotransmission In Vivo by Targeting Hippocampal Synapses

Rossana Rauti<sup>†</sup>, Manuela Medelin<sup>†,\*</sup>, Leon Newman<sup>¥</sup>, Sandra Vranic<sup>¥</sup>, Giacomo Reina<sup>§</sup>, Alberto Bianco<sup>§</sup>, Maurizio Prato<sup>‡,¶,Δ</sup>, Kostas Kostarelos<sup>¥#</sup>, Laura Ballerini<sup>†#</sup>

<sup>†</sup>Neuron Physiology and Technology Lab, International School for Advanced Studies (SISSA), Neuroscience, Trieste, Italy

<sup>\*</sup>Life Science Department, University of Trieste, Italy

<sup>¥</sup>Nanomedicine Lab, Faculty of Biology, Medicine & Health and National Graphene Institute, AV Hill Building, University of Manchester, Manchester, United Kingdom

<sup>§</sup>University of Strasbourg, CNRS, Immunology, Immunopathology and Therapeutic Chemistry, UPR 3572, 67000 Strasbourg, France

<sup>‡</sup>Department of Chemical and Pharmaceutical Sciences, University of Trieste, Trieste, Italy

<sup>¶</sup>Nanobiotechnology Laboratory, CIC biomaGUNE, San Sebastián, Spain

<sup>Δ</sup>Ikerbasque, Basque Foundation for Science, Bilbao, Spain

**KEYWORDS:** graphene, synapses, hippocampal network, glutamate, quantum dots.

18

## 19 ABSTRACT

20 Synapses compute and transmit information to connect neural circuits and are at the basis of brain  
21 operations. Alterations in their function contribute to a vast range of neuropsychiatric and  
22 neurodegenerative disorders and synapse-based therapeutic intervention, such as selective  
23 inhibition of synaptic transmission, may significantly help against serious pathologies. Graphene  
24 is a two-dimensional nanomaterial largely exploited in multiple domains of science and  
25 technology, including biomedical applications. In hippocampal neurons in culture, small graphene  
26 oxide nanosheets (s-GO) selectively depress glutamatergic activity without altering cell viability.  
27 Glutamate is the main excitatory neurotransmitter in the central nervous system and growing  
28 evidence suggests its involvement in neuropsychiatric disorders. Here we demonstrate that s-GO  
29 directly targets the release of pre-synaptic vesicle. We propose that s-GO flakes reduce the  
30 availability of transmitter, via promoting its fast release and subsequent depletion, leading to a  
31 decline of glutamatergic neurotransmission. We injected s-GO in the hippocampus in vivo, and  
32 forty-eight hours after surgery ex vivo patch-clamp recordings from brain slices show a significant  
33 reduction in glutamatergic synaptic activity, in respect to saline injections.

34

35

36

37

38

39 Graphene is a 2D material made of  $sp^2$ -hybridized carbon atoms organized in a hexagonal lattice  
40 and characterized by excellent physical features, including outstanding electron mobility and  
41 mechanical flexibility.<sup>1-3</sup> Because of its properties,<sup>4-6</sup> graphene is considered a rising star in a  
42 growing number of technological developments, including biomedical ones.<sup>2,4,5,7</sup> In neurology,  
43 graphene-based neuronal implants or bio-devices, may overcome current technical limitations in  
44 treating pathologies that range from neurooncology to neuroregeneration.<sup>8,9</sup> We reported recently  
45 the ability of small, thin graphene oxide sheets (s-GO) to alter specifically neuronal synapses, with  
46 no impact on cell viability. In particular, in cultured hippocampal networks, upon chronic long-  
47 term exposure to s-GO, glutamatergic release sites were sized down.<sup>10</sup> It is well known that  
48 glutamate is the main excitatory neurotransmitter in the mammalian central nervous system (CNS)  
49 and mediates neuronal development, migration, synaptic maintenance and transmission.<sup>11-13</sup> An  
50 uncontrolled release of glutamate in the extracellular space may lead to excitotoxicity,  
51 neurodegeneration and neurological disorders, including pain.<sup>14</sup> Localized targeting and fine-  
52 tuning of the glutamatergic system are attractive objectives in neuroscience. To achieve a deep  
53 understanding of the interactions between s-GO and the machinery governing nerve cell functions  
54 is mandatory to translate these findings into potential therapeutic applications. In particular,  
55 graphene translocation or adhesion to cell membranes<sup>15,16</sup> may potentially interfere with activities  
56 such as the exocytic and endocytic trafficking systems, essential to physiological synaptic  
57 transmission.<sup>15,17</sup> Here, we describe, by single cell electrophysiology, how s-GO nanosheets  
58 acutely tune synaptic release in excitatory synapses of hippocampal cultured neurons and acute  
59 slices, by interfering with the probability of vesicle release. We propose that such interference  
60 leads to transmitter depletion and subsequent depression of the glutamatergic activity. We next  
61 address whether such material similarly affects glutamatergic transmission in vivo, by injecting s-

GO in the dentate gyrus of the hippocampus of juvenile rats. We patch-clamped single neurons from ex vivo hippocampal slices, 48 h and 72 h after s-GO microinjections. We demonstrate that s-GO targets and down-regulates glutamatergic synapses in vivo and further illustrates the potential of s-GO flakes to be engineered as specific synaptic transmission modulators.

**GO functionalization and characterization.** The produced s-GO dispersion was visually homogenous and of a brownish-translucent appearance. The dispersions did not show any evidence of sedimentation or any other observable changes for over 6 months, indicating their physical stability. The characterization of the s-GO nanosheets is presented in Figure 1 and in Supplementary Figure S1. The morphological features of the s-GO nanosheets were examined using AFM (Figure 1a) and TEM (Supplementary Figure S1a). Both analytical methods showed that the lateral dimension of the s-GO nanosheets was predominantly between 100–300 nm with very few larger sheets into the  $\mu\text{m}$  range (Figure 1b). Moreover, AFM revealed that the material is composed of sheets from single to few-layer thickness (Supplementary Figure S1b). The material structural features were studied by Raman spectroscopy which evidenced the presence of the characteristic G and D scatter bands at  $1595\text{ cm}^{-1}$  and  $1330\text{ cm}^{-1}$ , respectively (Figure 1c). The D scatter band was markedly higher than the G band. The intensity ratio of these two peaks, known as the  $I(\text{D})/I(\text{G})$ , was calculated to be  $1.31 \pm 0.01$ , indicating that the material hexagonal lattice was defected. XPS analysis corroborated to the presence of functional groups (Supplementary Figure S1c) and further indicated that the defects correspond to oxygen-containing functionalities. The C/O ratio was found to be 2.1 and the material chemical purity was 99.8 %.<sup>18</sup> The surface functionalization was further supported by laser Doppler electrophoresis to indicate that the dispersed sheets had a surface charge of  $-55.9 \pm 1.4\text{ mV}$ . Aiming to track the s-GO flakes within neuronal tissue we performed covalent labeling of s-GO with quantum dot (QD) luminescent

nanoparticles. For this purpose, we first synthesized the AgInS<sub>2</sub>/ZnS-doped QDs capped with cysteine as described in the literature (see TEM images in Supplementary Figure S1d).<sup>19,20</sup> Subsequently, the coupling with s-GO was achieved via epoxy ring opening with the amino groups of the cysteine-capping agent. TEM microscopy shows the presence of small dark dots on the s-GO sheets associated with the presence of QDs on the surface (Supplementary Figure S1e, indicated by the arrows) as confirmed by XPS survey analysis (Figure 1d). The UV-Vis spectrum (Figure 1e) of the functionalized material showed a broadening of the absorption band between 300 and 600 nm due to the presence of the nanocrystals onto GO. Fluorescence characterization is reported in Figure 1f; s-GO showed an emission centered at 585 nm attributed to the electronic transitions from the bottom of conductive band and the nearby localized states to the valence band.<sup>21</sup> QDs have an emission centered at 706 nm due to transition between the conductive band and the defected carbon lattice.<sup>22</sup> Interestingly, when QD were coupled to graphene oxide only s-GO luminescence was detected. The quenching of the QD emission may be attributed to an interfacial electron transfer between the QDs and the s-GO surface due to their close proximity.<sup>23,24</sup> Surprisingly, the emission band centered at 585 nm, attributed to the GO photoluminescence, appeared stronger in the case of QD-s-GO than in non-modified s-GO. Most probably, the energy transfer process causes the decrease of donor emission (QD quenching) and increase the s-GO acceptor emission<sup>24</sup> allowing us to visualize the s-GO-QD in the biological environment (vide infra).

**s-GO targets synaptic vesicle release at glutamatergic synapses in cultured hippocampal neurons.** To unravel the mechanisms by which thin s-GO sheets affect neurotransmission, we patch-clamped cultured hippocampal neurons while a second pipette for the local delivery of standard saline solution of s-GO (100 µg/mL; see Methods) was positioned at 200 µm distance (by

108 microscopic guidance) from the recorded neuron (sketched in Figure 2a). We estimated that, at  
 109 this distance, the application of a brief (500 ms) pulse of pressure should result in a local (i.e. on  
 110 the patched cell) and transient delivery of s-GO at a concentration of at least 10 % of that contained  
 111 in the pipette (see Methods). Spontaneous synaptic activity was recorded in the presence of  
 112 Tetrodotoxin, (TTX; 1  $\mu$ M). In TTX, synaptic events, termed miniature post synaptic currents  
 113 (mPSCs), reflect the pre-synaptic, stochastic release of vesicles at individual synaptic terminals  
 114 impinging on the recorded neuron. mPSCs frequency reflects the pre-synaptic release probability  
 115 and on the number of synaptic contacts, while mPSCs amplitude is dictated by postsynaptic  
 116 receptor sensitivity.<sup>25</sup> Baseline mPSCs were sampled before and after the local ejection of saline  
 117 or s-GO (Figure 2b). In cultured neurons, virtually all mPSCs were made up by excitatory (AMPA  
 118 glutamate receptor-mediated) events, identified by their fast kinetics (decay time constant  $\tau = 5 \pm$   
 119 0.5 ms;<sup>26</sup>), and were thus named excitatory mPSCs (mEPSCs). Figure 2b shows representative  
 120 control (top) and s-GO (bottom) current tracings prior and after saline or s-GO solution,  
 121 respectively, were pressure ejected. In control neurons mEPSCs frequency did not change (from  
 122  $0.06 \pm 0.03$  Hz to  $0.065 \pm 0.04$  Hz after saline-ejection,  $n = 14$ ; bar plot in Figure 2c, left). On the  
 123 contrary, acute s-GO ejection significantly increased (\*  $P < 0.05$  Student's t-test) the mEPSCs  
 124 frequency (from  $0.04 \pm 0.01$  Hz to  $0.12 \pm 0.02$ ,  $n = 13$ ; bar plot in Figure 2c, left). The increase in  
 125 mEPSCs appeared with 8-10 s delay from the local s-GO ejection and completely reversed to  
 126 baseline values ( $0.04 \pm 0.01$  Hz) 8-9 min following the acute application (bar plot in Figure 2c,  
 127 left). In all treatments, the mEPSCs amplitude was not affected (bar plot in Figure 2c, right). These  
 128 transient changes in the frequency of mEPSCs suggest a direct interference of s-GO with the  
 129 presynaptic release machinery<sup>27,28</sup> and are consistent with the hypothesized targeting by s-GOs of  
 130 endo-exocytotic mechanisms. This hypothesis is also validated by the co-localization of bassoon

(pre-synaptic terminal marker<sup>29</sup>) and s-GO detected by confocal microscopy in a different set of experiments, where s-GO was incubated (20  $\mu$ g/mL; 30 min), before fixation of the cultures (see Methods; Supplementary Figure S2 a and b, controls and s-GO, respectively). We further address the dependency of these effects on the flakes' size. We adopted the same protocol to press-eject GO flakes (same concentration as s-GO) characterized by different lateral dimensions: large GO (l-GO,  $\approx$  2  $\mu$ m) or ultra-small GO (us-GO,  $\approx$  40 nm).<sup>18</sup> Supplementary Figure S2 c shows representative control (top) and l-GO (bottom) current tracings sampled before and after the local ejection of saline or l-GO solutions. Opposite to s-GO, l-GO did not change mEPSCs frequency (from  $0.06 \pm 0.01$  Hz to  $0.07 \pm 0.02$  Hz after saline ejection,  $n = 5$ ; from  $0.05 \pm 0.01$  Hz to  $0.07 \pm 0.02$  Hz after l-GO ejection,  $n = 5$ ). Similarly (Supplementary Figure S2 d), us-GO did not modulate mEPSCs frequency (from  $0.05 \pm 0.01$  Hz to  $0.07 \pm 0.02$  Hz, after saline,  $n = 8$  and from  $0.05 \pm 0.01$  Hz to  $0.07 \pm 0.02$  Hz, after us-GO,  $n = 8$ ).

Thus only s-GO transiently increased the frequency of mEPSCs. This apparent discrepancy with our previous results, where prolonged exposure to s-GO decreased glutamatergic activity,<sup>10</sup> may be explained by the emergence of glutamate depletion due to forced glutamate release. The latter leading to a transient facilitation followed, when s-GO is applied longer than the duration of the facilitatory effects, by a depression of vesicle release and thus a down-regulation of glutamate transmission.<sup>10</sup>

To investigate the s-GO interference with presynaptic release and whether this was truly selective for excitatory synapses, we tested the local delivery of s-GO nanosheets on the occurrence of evoked PSCs (ePSCs), by simultaneous whole-cell recordings from two monosynaptically connected neurons.<sup>26</sup> Action potentials were induced in the presynaptic neuron and the evoked postsynaptic unitary PSCs (delay 2 ms) were examined. In our in vitro system, monosynaptically

154 coupled pairs of neurons typically display either GABA<sub>A</sub> or glutamate AMPA receptor-mediated  
 155 evoked currents.<sup>26,30,31</sup> We identified the different populations of ePSCs on the basis of their kinetic  
 156 properties and pharmacology.<sup>26,32</sup> In fact, GABAergic ePSCs were characterized by a slow decay  
 157 time constant ( $\tau = 23 \pm 7$  ms,  $n = 15$  for each condition, control and s-GO; Figure 2d, left) and  
 158 were fully abolished by administration of 5  $\mu$ M Gabazine ( $n = 3$ ). Glutamatergic AMPA receptor–  
 159 mediated ePSCs displayed fast decay ( $\tau = 7 \pm 1.2$  ms,  $n = 7$  for each condition; Figure 2d, right)  
 160 and were further blocked by application of 10  $\mu$ M CNQX ( $n = 3$ ). To investigate the presynaptic  
 161 properties we adopted paired-pulse stimulation protocols.<sup>33,34</sup> In paired-pulse stimulation the  
 162 second response can be either facilitated or depressed. Usually, at a specific synapse, an increased  
 163 probability of neurotransmitter release will favor paired-pulse depression, while a decrease in the  
 164 release probability favors facilitation.<sup>33,35,36</sup> Thus, differences in postsynaptic responses to paired-  
 165 pulse stimulation indicate variations in presynaptic transmitter release.<sup>33,36–38</sup> To probe the changes  
 166 in efficacy of unitary ePSCs paired-pulse protocols were performed with short inter-stimulus  
 167 interval (50 ms). Figure 2d shows representative presynaptic pairs of action potentials (top) and  
 168 the corresponding monosynaptic GABAergic (left tracings) or glutamatergic AMPA receptor  
 169 (right) evoked currents (bottom) before and after s-GO local pressure ejection. We indirectly  
 170 assessed the GABA and glutamate release probability before and after saline (control) or s-GO  
 171 ejection by measuring the paired-pulse ratio (PPR, calculating the ratio between the mean peak  
 172 amplitude of the second and the first PSC<sup>37,38</sup>). In control GABAergic and glutamatergic ePSCs  
 173 the resulting PPR indicated the presence of paired pulse depression and did not change upon saline  
 174 solution applications (for GABA<sub>A</sub> receptor-mediated pairs:  $0.5 \pm 0.2$  before and  $0.6 \pm 0.2$  after  
 175 saline; for AMPA receptor-mediated pairs:  $0.5 \pm 0.1$  before and  $0.6 \pm 0.2$  after saline, plot in Figure  
 176 2d). When investigating the impact of s-GO ejection, we detected a reduction (on average – 32 %)



in the amplitude of the first glutamatergic ePSC and a significant difference (\*  $P < 0.05$  Student's t-test) in PPR, indicative of paired-pulse facilitation, while the PPR did not change in GABA<sub>A</sub> ePSCs (for AMPA mediated pairs:  $0.5 \pm 0.1$  before and  $2 \pm 0.9$  after s-GO; for GABA<sub>A</sub> mediated pairs:  $0.5 \pm 0.2$  before and  $0.65 \pm 0.2$  after s-GO; summarized in the bar plots in Figure 2d, bottom). Altogether these experiments strongly support a direct interference of s-GO flakes with synaptic vesicle release, with an initial high rate of release followed by a decline when s-GOs are applied longer<sup>10</sup> or when acting synergistically to the action potential-evoked activation of the exocytotic apparatus, ultimately depleting evoked release, typically reflected by changes in ePSC amplitude.<sup>39,40</sup> Notably, only glutamatergic synapses were targets of the s-GO.

**s-GO exposure specifically affects glutamatergic synapses in acute hippocampal slices.** Since cultured networks are simplified 2D models of immature brain circuits, we explored the ability of s-GO to regulate glutamate synaptic activity in acute hippocampal slices, thus scaling up the complexity of the tissue to the third dimension and testing more mature synapses. Single neuron patch-clamp recordings were obtained from visually identified pyramidal cells in the CA1 hippocampal region. A second pipette was again positioned at a distance of 200  $\mu\text{m}$  from the recorded cell (sketched in Figure 3a) and filled with standard saline solution or with s-GO (100  $\mu\text{g/mL}$ ). Baseline PSCs were recorded before and after the local saline or s-GO ejection. Figure 3b shows representative current tracings of controls (top) and s-GO (bottom) before and after saline or s-GO solutions, respectively, were pressure ejected. In neurons exposed to saline solution, spontaneous PSCs frequency did not change ( $6 \pm 2$  Hz before the pipette saline-ejection and  $5 \pm 1$  Hz after the pipette saline-ejection,  $n = 14$ ). On the contrary, acute s-GO ejection significantly increased (\*  $P < 0.05$  Student's t-test) the PSCs frequency (from a baseline of  $5 \pm 2$  Hz to a post ejection frequency of  $8 \pm 2$  Hz,  $n = 13$ ). The increase in PSCs after the local s-GO ejection was

reversible. In fact, PSC frequency fully returned to baseline values 7-8 min following the acute application. In all treatments, the PSC amplitude was not affected. We further dissected the nature of PSCs by the use of CNQX or Gabazine, isolating GABA<sub>A</sub> or AMPA receptor-mediated IPSCs or EPSCs, respectively. When EPSCs were measured after s-GO ejection, we detected a strong increase (\*  $P < 0.05$  Student's t-test) in their frequency when compared to the saline solution pressure application ( $4 \pm 1$  Hz before and  $4.7 \pm 1$  Hz after the pipette saline-ejection;  $4.2 \pm 0.9$  Hz before and  $7.3 \pm 1$  Hz after the s-GO ejection, Figure 3c). On the contrary, when we measured IPSCs, their frequency was not affected both by saline ( $4.2 \pm 1$  Hz before and  $4.8 \pm 1$  Hz after, Figure 3d) and s-GO ( $3.8 \pm 1$  Hz before and  $4.2 \pm 1$  Hz after, Figure 3d) pressure applications. Such results support the notion of s-GO ability to specifically target excitatory synapses, even in tissue explants. In cultured neurons as well as in acute hippocampal slices, the brief pressure ejection of s-GO transiently increased the excitatory activity, apparently affecting glutamate release machinery at the presynaptic site.

To ascertain whether prolonged interference of s-GO with excitatory synapses might indeed reduce the activity of synapses capable of releasing glutamate, as observed in dissociated cultures<sup>10</sup> we incubated acute slices with s-GO (50  $\mu$ g/mL) and we monitored PSCs frequency after 30 min ( $n = 5$ ), 45 min ( $n = 5$ ), 3 h ( $n = 5$ ) and 6 h ( $n = 8$ ). Under these experimental conditions, s-GO will be repeatedly presented at synapses, in the absence of the fast clearance brought about by saline flow rate in the previous experiments (see Methods). The plots in Figure 3e compare the frequencies of PSCs in Control and s-GO treated samples against 4 different exposure time points. A progressive reduction in PSCs frequency was observed from 30 min to 6 h (from  $5.8 \pm 1$  Hz to  $3.6 \pm 0.8$  Hz), such changes were not detected in control (from  $5.0 \pm 1$  Hz to  $5.3 \pm 1$  Hz). In Figure 3e, by linear regression analysis of the two time progressions (Control and s-GO) combined to

multiple regression statistical analysis, we show that the zero slope hypothesis is accepted for Controls but not for s-GO, indicative of a significant progressive decrease in PSCs frequencies due to s-GO prolonged incubation.

**In vivo intra-hippocampal s-GO delivery reversibly reduces glutamatergic synaptic activity**

**in juvenile rats with minimal tissue reaction.** To gain more insights into the synapse specificity,

tissue reactivity and kinetics of s-GO in vivo, we injected in juvenile rats (P15) 1  $\mu$ L of s-GO (50  $\mu$ g/mL in saline solution; Figure 3f) in the dentate gyrus of the hippocampus and we patch-clamped

single neurons to measure glutamatergic synaptic activity from ex vivo hippocampal slices isolated

after 48 h and 72 h after the brain surgeries. As control, we injected 1  $\mu$ L of saline solution in the

same anatomical region. Figure 3f shows representative current tracings of the recorded electrical

activity in acute slices isolated from the contralateral (not subjected to the injection), the control

saline- and s-GO-injected hemispheres, after 48 h from injection. After this time period

hippocampal slices isolated from s-GO treated animals showed a clear and significant (\*\*  $P < 0.01$

two-way ANOVA) reduction in PSCs frequency ( $2 \pm 0.5$  Hz,  $n = 7$ ), when compared with slices

from the contralateral untreated hemisphere ( $5 \pm 1$  Hz,  $n = 9$ ) or with saline treated ones ( $4.3 \pm 1$

Hz,  $n = 8$ ; see plot in Figure 3g). Remarkably, such effects were reversible: upon 72 h recovery

post injections the reduction in synaptic PSCs frequency in s-GO treated slices is absent ( $6 \pm 1.3$

Hz,  $n = 8$  for contralateral slices;  $5.7 \pm 1.5$  Hz,  $n = 7$  for saline-injected slices;  $6.2 \pm 1.8$  Hz,  $n = 7$

for s-GO-injected slices; see plot in Figure 3g). In all treatments, the PSCs amplitude was not

affected. When pharmacologically discriminating GABA<sub>A</sub> and AMPA receptor-mediated PSCs,

we specifically detected after 48 h of s-GO a significant (\*  $P < 0.05$  two-way ANOVA) reduction

in EPSCs frequency ( $2.9 \pm 0.8$  Hz,  $n = 7$ ), when compared with slices from the contralateral

untreated hemisphere ( $4.8 \pm 1$  Hz,  $n = 9$ ) or with saline treated ones ( $5 \pm 1.3$  Hz,  $n = 8$ ; see right

246 plot in Figure 3h). GABA<sub>A</sub> receptor-mediated PSCs were not affected by any treatment (from  $3.5 \pm 1$  Hz to  $3.9 \pm 0.8$  Hz after saline-ejection,  $n = 8$ , and from  $3 \pm 0.5$  Hz to  $3.4 \pm 0.5$  Hz after s-GO-  
 247 ejection;  $n = 7$ ). To prove the presence of s-GO and gain more insight regarding its fate within the  
 248 hippocampus in vivo, we used bright field microscopy with correlative Raman based mapping  
 249 (Figure 4a). Forty-eight h following intra-hippocampal delivery ( $50 \mu\text{g/mL}$  final concentration;  $1 \mu\text{L}$  injected volume), the presence of s-GO could be positively identified within the  $20 \mu\text{m}$  sections  
 250 of injected hippocampi, specifically within the confines of the dentate gyrus. However, 72 h post  
 251 injection, the material presence is shown to decrease. We also tested the hippocampi of rats that  
 252 were injected with a saline control and a higher concentration of s-GO ( $1.3 \text{ mg/mL}$ ;  $1 \mu\text{L}$ ), which  
 253 served as negative and positive controls, respectively, to verify our data. The localization of s-GO  
 254 by using QD-s-GO ( $50 \mu\text{g/mL}$ ;  $1 \mu\text{L}$ ) was performed next. Figure 4b shows the  
 255 immunofluorescence labeling of slices isolated from the treated hippocampus where the area of  
 256 injection is highlighted by the typical microglia reaction (Iba1 positive cells in green) due to the  
 257 surgery per se.<sup>41,42</sup> QD-s-GO was typically localized in the area of injection after 24 h (red  
 258 staining). Next we investigated whether s-GO injection was affecting the number of synapses in  
 259 the injected brain area. We used bassoon marker for pre-synaptic terminals present in both  
 260 glutamatergic and GABAergic synapses.<sup>29</sup> We quantified the co-localization of bassoon with  
 261 neurons (labeled with  $\beta$ -tubulin III) and we did not detect any difference between saline and s-GO  
 262 treated (48 h) animals in terms of bassoon volume at the injection site (saline  $552.68 \pm 155.06 \mu\text{m}^3$   
 263 and s-GO  $570.40 \pm 115.74 \mu\text{m}^3$ ; number of animals = 2 for each experimental group; Figure 4c,d).  
 264 To investigate tissue reactivity, in particular neuroglia responses, to s-GO following 48 h and 72  
 265 h, we performed immunohistochemistry experiments on treated animals to identify GFAP-positive  
 266 astrocyte and Iba1-positive microglia (number of animals = 3 for each experimental group; Figure

5a,b). We measured astrocytes and microglia located 300  $\mu\text{m}$  apart to the injection site in the medial and lateral directions, at such a distance we detected only a low tissue response in all groups (Figure 5c,d). Conversely, at the injection site the tissue reactivity was higher, as expected,<sup>41,42</sup> yet comparable between saline and s-GO. To note, astrocyte recruitment was decreased in s-GO treated animals, particularly after 48 h; while microglia reactivity was similar in saline and s-GO groups after 48 h, but it was significantly lower in s-GO treated animals after 72 h (Figure 5; \*\*  $P < 0.01$ ; two-way ANOVA).

We report here the ability of s-GO nanosheets to interact selectively with glutamatergic synapses, affecting the efficacy of neurotransmission, *in vitro* and *in vivo*. In particular, in cultured hippocampal neurons, brief exposures to s-GO promote an initial high rate of glutamate quantal release, presumably by modifications at the pre-synaptic site, as indicated by the increase in frequency of spontaneous mEPSCs<sup>25,43,44</sup> and by the paired-pulse experiments.<sup>33,35-38</sup> We hypothesize that this initial high rate of release depletes presynaptic glutamate and, in the continuous presence of s-GO, inhibit glutamatergic transmission. Indeed, in the same preparation, the decline in action potential-evoked monosynaptic EPSCs upon s-GO exposure supports the notion of a subsequent reduction in the probability of release following vesicle depletion<sup>45</sup> brought about by s-GO. In all tests, the mere pressure ejection of saline solution without s-GO, or GO of different dimensions, did not change spontaneous or evoked synaptic responses. Notably, GABAergic synapses were never affected. The bi-phasic effects of s-GO, characterized first by a transient increase in neurotransmitter release which, upon a potential reduction in the vesicle-pool size, is followed by a depression, hints at the ability of s-GO to engage the presynaptic exocytotic machinery, as also supported by the co-localization with pre synaptic terminal markers. Neurotransmitter release, at the presynaptic site in the CNS, is controlled by specific proteins that

292 function in large complexes, displaying multiple roles in synaptic vesicle recycling.<sup>46</sup> In addition  
 293 to release-proteins another potential target of s-GO is represented by intracellular  $\text{Ca}^{2+}$  levels,  
 294 known to regulate evoked neurotransmitter release<sup>45</sup> and recently reported to be modulated by  
 295 chronic exposure to s-GO.<sup>47</sup> Although we cannot exclude a role of presynaptic  $\text{Ca}^{2+}$  influx  
 296 contributing to acute s-GO effects, the detected increase in spontaneous miniature current  
 297 frequency, much less dependent on  $\text{Ca}^{2+}$  levels,<sup>44,48</sup> and the absence of modulation by s-GO of the  
 298 GABAergic terminals, usually regulated by presynaptic  $\text{Ca}^{2+}$  dynamics<sup>49</sup>, are suggestive of a  $\text{Ca}^{2+}$   
 299 independent mechanisms. The responses evoked by pressure ejected s-GO are reminiscent to those  
 300 induced by hypertonic solutions<sup>50</sup>, however a simple osmotic mechanism is ruled out by the  
 301 selectivity of the effects (restricted to glutamatergic terminals) observed in all conditions tested  
 302 and by direct osmotic pressure measures (see Methods). The current data are in agreement with  
 303 our previous report, where a long-term (days) exposure to s-GO selectively down regulated  
 304 excitatory neurotransmission leaving inhibitory synapses unchanged.<sup>10</sup> We previously  
 305 speculated<sup>10</sup> that differences in GABAergic and glutamatergic synaptic cleft ultrastructure, in  
 306 particular in the cleft size and organization<sup>51</sup>, might explain why the latter terminals became ideal  
 307 targets to s-GO interactions. To note, larger or smaller GO flakes did not modulate glutamate-  
 308 mediated synaptic transmission. In this framework, we propose a simply mechanistic interpretation  
 309 of our current experiments: glutamatergic synapses, in virtue of their relatively larger size and less  
 310 structured organization,<sup>51</sup> allow penetration of s-GO flakes which remain trapped within the cleft  
 311 and adhere to the plasma membrane at active release sites. GO nanosheets have been suggested to  
 312 adhere to complex patches of cellular membranes, rather than specific ones.<sup>52</sup> Also in our  
 313 experiments, the s-GO adhesion to the membrane may be supported by non-specific interactions  
 314 (as described in other cell types<sup>52</sup>) accompanied by variable degrees of membrane deformations, a

315 mechanism further supported by our previous results showing astrocyte vesicle shedding when  
316 exposed to s-GO.<sup>10</sup> A deformation of synaptic active zones would interfere with the exocytosis  
317 and neurotransmitter vesicle release by a mechanical mechanism reminiscent of, for example,  
318 stress induced ones,<sup>50</sup> not necessarily implying an impairment of membrane integrity. In fact, we  
319 never observed any functional sign of membrane damage, and in addition the alterations in vesicle  
320 release were reversible. An alternative mechanism, due to the physical properties of nanoparticles,  
321 is related to their surface potential, able to tune neuronal excitability.<sup>53</sup> We previously documented  
322 that the s-GO surface potential, measured as zeta potential value<sup>10</sup>, is negative (– 50 mV), thus the  
323 negative charge may favor the s-GO interactions with neuronal membrane influencing the  
324 excitability of neurons.<sup>53</sup> Although we cannot exclude this mechanism, the short- and long- term  
325 regulation and the selectivity for excitatory synapses are not explained by this interpretation. The  
326 interface between dispersed s-GO sheets and the cell membrane is currently subject to active  
327 investigation, due to its potential in modulating cellular mechanosensing for diverse biomedical  
328 applications, nevertheless the nature of such interactions is still elusive.<sup>52,54</sup> Synaptic vesicle  
329 recycling machinery represents a feasible therapeutic target, regardless of the direct involvement  
330 of presynaptic function in a pathological process. Even subtle alterations in (pre)-synaptic  
331 communication hold the potential to compensate for deficits without interfering with postsynaptic  
332 signaling. Pre-synaptically targeted drug development might be challenging due to the  
333 sophisticated molecular complexity of the release machinery. The ability of s-GO to specifically  
334 hook glutamatergic presynaptic nerve terminals is thus highly promising, however conventional  
335 2D cultures may lack appropriate cell-extracellular matrix interactions, providing an artificially  
336 higher access of exogenous agents to synapses. s-GO specificity towards glutamatergic synapses  
337 may be virtually restricted to 2D bio-system models. This potential pitfall is excluded by our

experiments on acute hippocampal slices, the neuroscientist gold standard to investigate synaptic functions in intact circuitries. The selective effect of s-GO on glutamatergic transmission is preserved in tissue slices, where excitatory EPSCs are reversibly affected by s-GO, with a short-term up-regulation of release, turned into a down regulation upon prolonged exposure. The ultimate potential of any s-GO sheets in the design of therapeutic strategies based on synaptic targeting resides in testing their efficacy in vivo. We demonstrated the delivery of s-GO in vivo by stereotactic injection and we have shown that such an administration of s-GO (but not the surgery per se) in the hippocampus of juvenile rats significantly and selectively sized down glutamatergic activity, in the absence of direct reduction in the number of synapses. We have also shown that local tissue responses to stereotactic injections<sup>41,42</sup> were not increased by the presence of s-GO in terms of patterns of microglia together with astrocyte aggregation at the injection site. These results are supportive of, within the concentrations tested, the in vivo biocompatibility of the s-GO dispersions. In general, GO is characterized by better biocompatibility when compared to other types of graphene (such as pristine graphene or reduced GO) and additional functionalization might even further reduce the risk of inflammation and subsequent tissue toxicity.<sup>55</sup> Interestingly, our results also suggest a possible anti-inflammatory effect by limiting the aggregation of astrocytes surrounding the stereotactic injection and lessening prolonged microglia reactivity.<sup>41,42</sup> This result, although preliminary, is in accordance with previous observations<sup>56</sup> and renders further investigation. Exploiting s-GO in pre-synaptic drug design development certainly requires additional studies, as well as to ascertain a more precise s-GO mechanism of action and clearance, since in our experiments, due to diffusion, perfusion flow rate in vitro, potential membrane recycling,<sup>57</sup> and microglial uptake<sup>58</sup> we probably had only a “local” tissue clearance. Besides, most of the studies evaluating the clearance in vivo of GO suggested that GO is rapidly



cleared, but have been performed in non-mammalian organisms.<sup>59,60</sup> In our proof-of-concept in vivo study the coherence between the low detection of residual s-GO at 72 h and the reversibility of the synaptic silencing upon 72 h are supportive of a direct, mechanical interaction at the pre-synaptic plasma membrane.

## Methods

**Graphene oxide nanosheets synthesis.** GO was manufactured under endotoxin-free conditions through our modified Hummers' method as previously described.<sup>10,61</sup> Briefly in this procedure, 0.8 g of graphite flakes was added to 0.4 g of sodium nitrate (Sigma-Aldrich, UK). This was next followed by the slow addition of 18.4 mL of sulfuric acid 99.999% (Sigma-Aldrich, UK). After a homogenized mixture was achieved through stirring, 2.4 g of potassium permanganate (Sigma-Aldrich, UK) were added and maintained for 30 min. Thereafter, 37 mL of water for injection (Fresenius Kabi, UK) were added. This resulted in an exothermic reaction. The temperature was strictly kept at 98 °C for 30 min. The mixture was next diluted with 112 mL of water for injection (Fresenius Kabi, UK). Twelve mL of 30% hydrogen peroxide (Sigma-Aldrich, UK) were then added to reduce the residual  $\text{KMnO}_4$ ,  $\text{MnO}_2$ , and  $\text{MnO}_7$  to soluble manganese sulphate salts. The resulting mixture purified by repeated centrifugation cycles at 9000 rpm for 20 min until an orange/brown gel-like layer of GO began to appear on at the pellet-supernatant interface which occurred at around pH 6-7. This layer was carefully extracted with warm water for injection (Fresenius Kabi, UK). This layer contained large GO sheets; the obtained material was diluted in water for injection to yield an aqueous suspension with a concentration of 2 mg/mL. A portion of this obtained material was then lyophilised, reconstituted in water for injection (Fresenius Kabi, UK) and then sonicated in a bath sonicator (VWR, 80W) for 5 min. The resulting dispersion was then centrifuged at 13000 rpm for 5 min at room temperature (RT); the supernatant which

contained the desired s-GO nanosheets was separated from the unwanted pellet. A thorough physico-chemical characterization of us-GO and l-GO has already been reported.<sup>18</sup> Structural properties such as lateral dimension and thickness of the GO materials were then studied by AFM and TEM. Raman spectroscopy and  $\zeta$ -potential measurements were used to define the materials surface properties. TGA was also performed to examine the functionalization degree of the s-GO sheets. Moreover, XPS was used to examine the composition of the GO sheets, C/O ratio, and the presence of the different functional groups.

**s-GO functionalization.** QD have been prepared according to the literature by controlled decomposition of Ag and In salts. Briefly, 88.4 mg of  $\text{InCl}_3$  (0.4 mmol, Sigma Aldrich) and 17 mg  $\text{AgNO}_3$  (0.1 mmol, Sigma Aldrich) were placed in a 100 ml round-bottom flask. Then, 190  $\mu\text{L}$  of oleic acid (0.6 mmol, Sigma Aldrich), 720  $\mu\text{L}$   $\square\square\square\square$  dodecylthiol (0.6 mmol, Sigma Aldrich) and 8 mL of 1-octadecene (Sigma Aldrich) have been added under argon. The solution was heated at 60 °C for 15 min, at 90 °C for 15 min, and left at 110 °C stirring till no precipitate was visible (15-30 min). Then, 4 mL of solution S (9.6 mg 0.3 mmol, Sigma Aldrich) was added and the mixture turned reddish. Finally, 5 mL of  $\text{ZnCl}_2$  solution (70.5 mg 0.5 mmol, Sigma Aldrich) in oleylamine and 1-octadecene were added and the temperature was raised to 150 °C. After 15 min, the reaction was cooled with an ice bath. The QDs were purified by precipitation with ethanol, re-suspended with cyclohexane, washed several times with ethanol/acetone and stored in  $\text{CH}_2\text{Cl}_2$ . For the water transfer reaction, 2 mL of solution oil QDs (2 mg/mL dispersion) have been added to 1 mL of a cysteine (50 mg 0.4 mmol) basic solution in methanol. Immediately, the QD precipitated. After 20 min, 5 mL of distilled water have been added and the QD passed throw the aqueous phase. Subsequently, the water soluble QDs have been precipitated with acetone, washed several times with acetone/ethanol and stored in distilled water. For GO conjugation QDs have been mixed with

GO (1 mg/mL) at 1/10 mass ratio in distilled water. The mixture has been left stirring for 3 days and then purified via dialysis against distilled water.

**Preparation of hippocampal cultures and acute hippocampal slices.** Primary hippocampal cultures were prepared from neonatal rats at 2-3 postnatal days (P<sub>2</sub>-P<sub>3</sub>) as previously reported.<sup>10,26,62</sup> All procedures were approved by the local veterinary authorities and performed in accordance with the Italian law (decree 26/14) and the UE guidelines (2007/526/CE and 2010/63/UE). The animal use was approved by the Italian Ministry of Health. All efforts were made to minimize suffering and to reduce the number of animals used. All chemicals were purchased by Sigma-Aldrich unless stated otherwise. Cultures were then used for experiments after 8 ÷ 12 days in vitro. Hippocampal acute slices were obtained from P<sub>7</sub>-P<sub>8</sub> rats and from juvenile P<sub>15</sub> rats (n = 18 animals) using a standard protocol.<sup>63,64</sup>

**Electrophysiological recordings.** In dissociated hippocampal cultures, single and paired whole-cell recordings were obtained with pipettes (5-7 MΩ) with the following intracellular saline solution (in mM): 120 K gluconate, 20 KCl, 10 HEPES, 10 EGTA, 2 MgCl<sub>2</sub>, 2 Na<sub>2</sub>ATP, pH 7.3; osmolarity 300 mOsm. The extracellular saline contained (in mM) 150 NaCl, 4 KCl, 1 MgCl<sub>2</sub>, 2 CaCl<sub>2</sub>, 1 MgCl<sub>2</sub>, 10 HEPES, 10 glucose, pH 7.4. Data were recorded by Multiclamp 700B patch amplifier (Axon CNS, Molecular Devices) digitized at 10 KHz by pClamp 10.2 software (Molecular Devices LLC, USA). Basal PSCs were recorded at – 56 mV holding potential (liquid junction potential of 14 mV was not corrected for). mPSCs were recorded in the presence of TTX (1 μM) to block fast voltage-dependent sodium channels. In voltage-clamp recordings, PSCs and mPSCs were detected by the use of the AxoGraph X (Axograph Scientific) event detection program and by the Clampfit 10 software (pClamp suite, Axon Instruments) as previously reported<sup>64</sup>. On average, ≥ 500 PSCs were analyzed from each cell and from the average of these

430 events we measured the peak amplitude and the decay time constant (expressed as  $\tau$ ) by fitting a  
 431 mono-exponential function. In paired recordings, the presynaptic neuron in current clamp mode  
 432 was held at  $-70$  mV (by  $\leq 0.02$  nA negative current injection), and action potentials were evoked  
 433 by delivering short (4 ms) square current pulses (1 nA). Monosynaptic connections were identified  
 434 by their short delay ( $< 2$  ms)<sup>64</sup>. To characterize the short-term dynamics of synaptic contacts, we  
 435 delivered, to pairs of connected neurons, paired pulse stimulations at 20 Hz (1 pair every 20 s; 10  
 436 times, that were pooled together and averaged). For acute hippocampal slices, a patch-clamp  
 437 amplifier (Multiclamp 700B, Axon Instruments, Sunnyvale, CA, USA) allowed recordings from  
 438 CA1 pyramidal neurons, identified by visual inspection at an upright microscope (Eclipse FN1;  
 439 Nikon, Japan) equipped with differential interference contrast optics and digital videocamera  
 440 (Nikon, Japan). All recorded events were analyzed offline with the AxoGraph 1.4.4 (Axon  
 441 Instrument) event detection software (Axon CNS, Molecular Devices). s-GO was acutely  
 442 delivered<sup>10</sup>, both in dissociated cells and in acute hippocampal slices, by an injection of pressurized  
 443 air (500 ms duration, 8 PSI; by a Picospritzer PDES-02DX; NPI electronic GmbH, Germany).  
 444 Once patch-clamped neurons, a second pipette identical to that used for patch-clamp recording,  
 445 was positioned at a distance of 200  $\mu$ m (under microscopy control) from the recorded cell. The  
 446 pipette was filled with standard saline solution (control; osmolarity 300 mosmol l<sup>-1</sup>) or with s-GO,  
 447 l-GO and us-GO (100  $\mu$ g/mL in Krebs solution; osmolarity 300 mosmol l<sup>-1</sup>). The concentration of  
 448 GO reaching the cell was at least 10 % of that contained in the pipette, considering 1 mL of  
 449 extracellular solution in the recording chamber. Baseline PSCs were sampled before (10 min) and  
 450 after (10 min) the local ejection. Analyses were performed between 4 min and 8 min after the local  
 451 ejection, sampling 2 min of recordings.

**Confocal microscopy in hippocampal cultures.** Cultured hippocampal neurons (3 cultures; 6-8 DIV) were incubated for 30 minutes with s-GO (20 µg/mL). Cultures were then fixed by 4 % formaldehyde (prepared from fresh paraformaldehyde; Sigma) in PBS at RT and blocked and permeabilized in 5 % fetal bovine serum (FBS), 0.3 % Triton-X 100 in PBS for 30 min at RT. Samples were incubated with primary antibodies (mouse monoclonal anti-bassoon, 1:400 dilution; rabbit anti-β-tubulin III, 1:500 dilution) diluted in PBS with 5 % FBS for 45 minutes. Cultures were finally incubated with secondary antibodies (Alexa 488 goat anti-mouse, Invitrogen, 1:500 dilution; Alexa 594 goat anti-rabbit, Invitrogen, 1:500 dilution) and DAPI (Invitrogen, dilution 1:200) to stain the nuclei, for 45 minutes at RT and finally mounted on 1 mm thick glass coverslips using the Fluoromount mounting medium (Sigma-Aldrich). To visualize s-GO localization was used the reflection mode of confocal microscopy.<sup>58</sup> Images were acquired using a Nikon C2 Confocal, equipped with Ar/Kr, He/Ne and UV lasers. Images were acquired with a 60 × (1.4 NA) oil-objective (using oil mounting medium, 1.515 refractive index). Confocal sections were acquired every 0.4 µm.

**Surgery and s-GO injection.** Four experimental groups were used: standard saline solution (control) and s-GO 50 µg/mL injection, analyzed at 48 h and 72 h. Surgery was performed in P<sub>15</sub> Wistar rats anesthetized with ketamine (60 mg/kg i.p.) and xylazine (10 mg/kg i.p.). All animal procedures were conducted in accordance with the National Institutes of Health, international and institutional standards for the care and use of animals in research, and after consulting with a veterinarian. All experiments were performed in accordance with the EU guidelines (2010/63/UE) and Italian law (decree 26/14) and were approved by the local authority veterinary service. All efforts were made to minimize animal suffering and to reduce the number of animal used. The Italian Ministry of Health, in agreement with the EU Recommendation 2007/526 /CE, approved

animal use (authorization n° 1135/2015-PR). Animals were fixed in a stereotaxic device (World Precision Instruments, WPI). An incision was made on the top of the head in order to expose the skull and identify bregma and lambda coordinates. The injection of 1  $\mu$ L of saline or s-GO solution (10 steps of 0.1  $\mu$ L every minute) was performed with a Hamilton syringe (26s gauge; Hamilton). The following coordinates were used to reach the left dentate gyrus: AP: -3.0, ML: -3.0, DV: -3.3 relative to bregma.<sup>65</sup> At the end of the last step, the syringe was left in situ for extra 5 minutes to optimize the solution permeation. The incision was sutured and animals were constantly monitored and left undisturbed until electrophysiological or histological experiments.

**Histology procedures.** After 48 h or 72 h, animals were anesthetized and sacrificed by intracardiac perfusion with 0.1 M PBS followed by 4 % formaldehyde (prepared from fresh paraformaldehyde; Sigma) in PBS. Brains were promptly removed, postfixed in the same fixative solution for 24 h at 4 °C, and cryoprotected in 30 % sucrose in PBS at 4 °C for 24-48 h. Finally, brains were embedded in optimal cutting temperature (OCT) compound (Tissue-Tek), frozen at – 20 °C, and sagittal sections (25  $\mu$ m) were obtained using a cryostat (Microm HM 550, Thermo Fisher Scientific) and processed for immunohistochemistry. Tissue-Tek was removed by PBS washing and tissue sections were protein-blocked in 3 % BSA, 3 % FBS and 0.3 % Triton X-100 in PBS for 45 minutes at RT. Sections were then incubated overnight at 4 °C with primary antibodies (mouse anti-GFAP, Sigma-Aldrich, 1:400; rabbit anti-Iba1, Wako, 1:500; rabbit anti- $\beta$ -tubulin III, Sigma-Aldrich, 1:500; mouse anti-Bassoon, Abcam, 1:400) in 5 % FBS in PBS. After washing in PBS, sections were incubated in secondary antibodies (goat anti-rabbit AlexaFluor 594, Thermo Fisher Scientific, 1:400; goat anti-mouse AlexaFluor 488, Thermo Fisher Scientific, 1:400) in 5% FBS in PBS for 2-4h at RT. Nuclei were labeled with DAPI (Thermo Fisher Scientific, 1:500) in PBS

for 20-30 minutes at RT. Upon final washing (PBS and water), tissue sections were mounted on glass coverslips using Vectashield mounting medium (Vector Laboratories).

**Image acquisition and analysis.** We measured the brain tissue reaction by markers for reactive astrocytes and microglia (GFAP and Iba1, respectively). Fluorescence images were acquired using a Leica DM6000 upright microscope with a  $10 \times$  dry objective. Identical binning, gains and exposure times were used for all images of the same marker. Image analysis was performed using Fiji software. For both GFAP and Iba1 intensity measurements, a single region of interest (ROI,  $1000 \times 500 \mu\text{m}^2$ ) was selected at the injection site (left dentate gyrus). The background intensity threshold was defined for each section using the labeling intensity measured in the contralateral hemisphere in the same anatomical region (right dentate gyrus). The area within each ROI with intensity above the background threshold was calculated, normalized to the contralateral hemisphere and used for statistics. The ROI for all sections were averaged for each experimental group. We performed this analysis also 300  $\mu\text{m}$  medial and lateral to the injection site. We visualized s-GO by linking QD. Fluorescence images were acquired using a Leica DM6000 upright microscope with a  $10 \times$  dry objective. We further analyzed the amount of synaptic contacts by a specific marker for synapses (bassoon) in two experimental groups: saline and s-GO injection at 48 h. Confocal images were acquired using a confocal microscope (Nikon C1) with a  $60 \times$  oil objective (N.A. 1.4, oil mounting medium refractive index 1.515). Z-stacks were acquired every 350 nm for a total thickness of 7  $\mu\text{m}$ . Identical binning, gain and exposure time was used for all images. 9 ROIs ( $70 \times 70 \mu\text{m}^2$ ) for each section were randomly selected at the injection site (left dentate gyrus). Offline analysis was performed using Volocity software (Volocity 3D image analysis software, PerkinElmer, USA). For each ROI, we used the Z-stack to quantify bassoon signal as 3D objects. From the resulting values, we calculated the volume of only bassoon objects

co-localized with the  $\beta$ -tubulin III labeling in order to identify genuine synapses at neuronal level.

The ROI for all sections were pooled together and averaged for each experimental group.

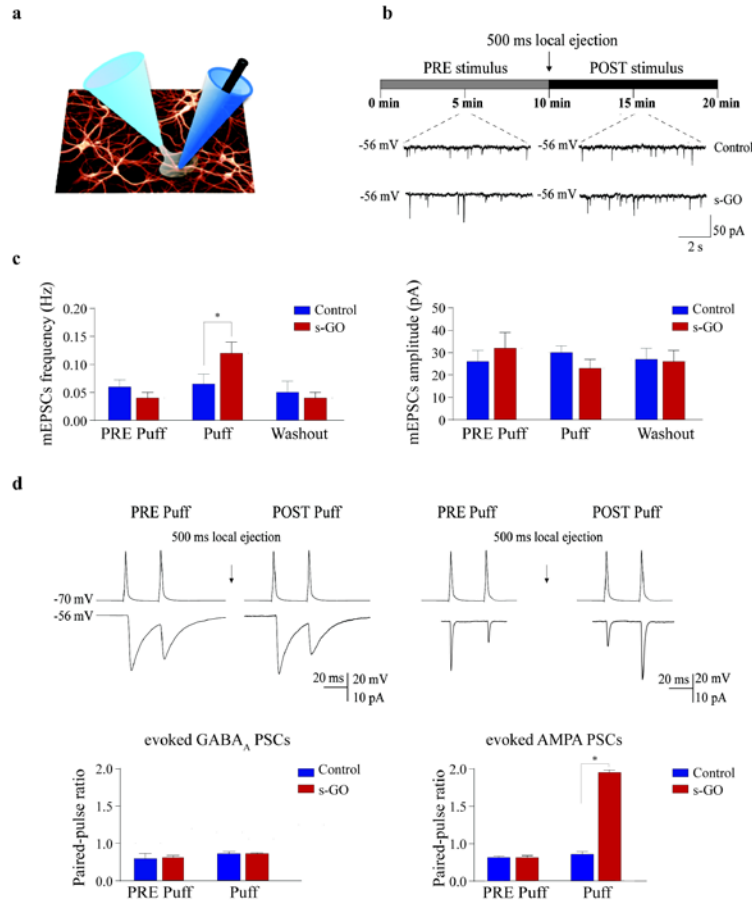
**Raman mapping of brain sections.** Raman mapping of sectioned brain samples was completed using a DXRi Raman Mapping system (Thermo Scientific, USA) using the following conditions:  $\lambda = 633$  nm, 1 mW, pixel size = 1.6  $\mu$ m and frequency = 25 Hz. The maps were generated according to the composite spectra's percentage similarity to a correlation GO spectral reference as shown.

**Statistical analysis.** All values from samples subjected to the same experimental protocols were pooled together and results are presented as mean  $\pm$  S.D., if not otherwise indicated; n = number of neurons, if not otherwise indicated. Statistically significant difference between two data sets was assessed by Student's t-test for parametric data. Differences between the logarithmic values of the analyzed variables were assessed using two-way ANOVA and multiple comparisons were adjusted by Bonferroni or Holm-Sidak correction. Statistical significance was determined at  $P < 0.05$ , unless otherwise indicated. Significance was graphically indicated as follows: \* $P < 0.05$ , \*\* $P < 0.01$ , \*\*\* $P < 0.001$ .



535

536 **Figure 1.** Characterization of s-GO. (a) AFM measure of s-GO sheets. (b) s-GO lateral  
537 dimension distribution. (c) S-GO Raman spectrum. (d) XPS survey of QD-s-GO. UV-vis (e) and  
538 fluorescence (f) spectra of s-GO, QD and QD-s-GO.



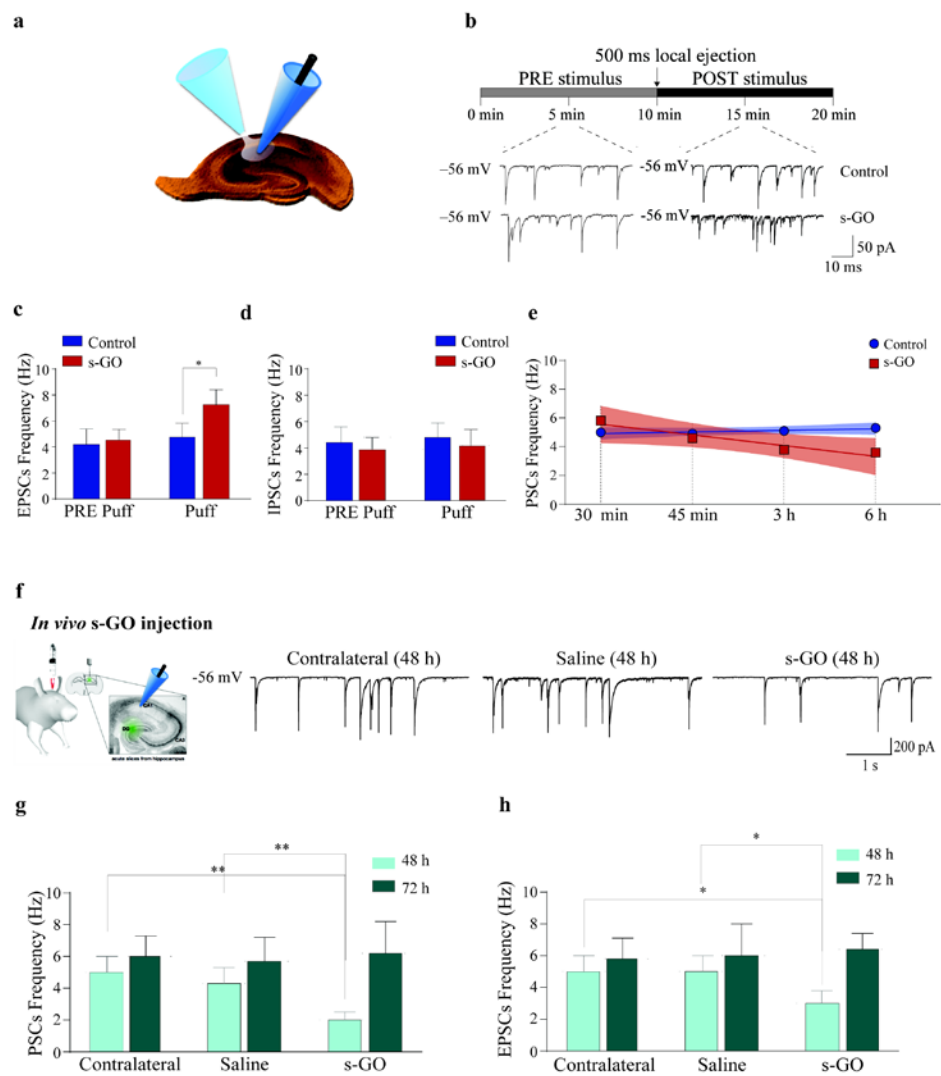
539

**Figure 2.** s-GO affects presynaptic glutamate release in hippocampal cultures (a) Sketch of the experimental setting for simultaneous s-GO pressure-release (puff) and single-cell recording from cultured neurons. (b) Top: diagram of the experimental protocol. Bottom: representative tracings of the spontaneous synaptic activity detected prior and after puff applications of control saline (Control, top) or s-GO (bottom). Recordings of mEPSCs are performed in the presence of TTX. In (c) bar plots of pooled data summarize the average mEPSCs frequency (left) and amplitude (right) before (PRE puff) and after (Washout) saline (Control) or s-GO (100  $\mu$ g/mL final concentration) pressure ejections (\*  $P < 0.05$  Student's t-test). Note the reversible increase in miniatures frequency due to s-GO. In (d) simultaneous pair recordings are shown: top traces represent presynaptic pairs (30 Hz) of action potentials, bottom ones the corresponding evoked monosynaptic PSCs (GABA<sub>A</sub>-receptor mediated on the left and glutamate AMPA-receptor mediated on the right) prior and after s-GO puffs. The paired-pulse ratios (PPR) measured prior and after saline solution (Control) and s-GO puffs are summarized in the histograms; note that s-

553 GO reduced the first evoked AMPA-receptor mediated PSCs and the PPR of glutamatergic  
554 synapses (\*P < 0.05 Student's t-test) supporting the notion of s-GO affecting presynaptic release.

555

556



557

**Figure 3.** EPSCs frequency modulation by s-GO in hippocampal slices *in vitro* and *in vivo* (a) Sketch of the experimental setting for simultaneous s-GO release and recording from hippocampal pyramidal cells. In (b) top: diagram of the experimental protocol. Bottom: representative current tracings recorded prior and after saline (Control; top) and s-GO (bottom) local pressure ejections. Glutamate AMPA-receptor mediated PSCs or GABA<sub>A</sub>-receptor mediated ones (EPSCs and IPSCs, respectively) were pharmacologically isolated and bar plots in (c) summarize the mean values of EPSCs and in (d) of IPSCs frequency before and after saline (Control) or s-GO puffs (\*P < 0.05 Student's t-test). Note that also in hippocampal slice explants only glutamatergic activity was transiently affected by brief local injection of s-GO. In (e) plots of pooled data represent the average PSCs frequency upon 30 min, 45 min, 3 h and 6 h s-GO incubation (50 µg/mL final concentration; Control: blue circles; s-GO: red squares). Note that prolonged incubation in s-GO depresses spontaneous synaptic activity. Linear regression analysis of the two time progressions is depicted as blue and red fitting lines ( $y = 4.91 + 0.11x$  for Control and  $y = 5.56 - 0.74x$  for s-GO, respectively) together with their corresponding confidence interval in pale blue and pale red, respectively. Regardless the significance of the difference between each two conditions at a specific time point (at 30 min P = 0.91, at 45 min P = 0.60, at 3 h P = 0.07, at 6 h P = 0.06), multiple regression statistical analysis revealed that the zero slope hypothesis is accepted for Controls but not for s-GO. The equal slope hypothesis between the two trends was instead rejected by a Tukey test on the two slopes. f) *In vivo* intra-hippocampal s-GO delivery reversibly reduces glutamatergic synaptic activity in adult rats: sketch of the experimental settings (left) and (right) spontaneous synaptic activity recorded from *ex vivo* hippocampal slices isolated from juvenile rats after 48 h from the surgery. Recordings were taken from the contralateral, control (saline) and s-GO (50 µg/mL final concentration) injected hemisphere after 48 h from surgery. In (g) bar plots summarize the PSCs and in (h) the EPSCs frequency in control and s-GO treated animals after 48 h and after 72 h from surgery (\*\*P < 0.001 two-way ANOVA; \*P < 0.05 two-way ANOVA). Note that the specific reduction in EPSC frequency at 48h that was entirely reversed at 72 h.

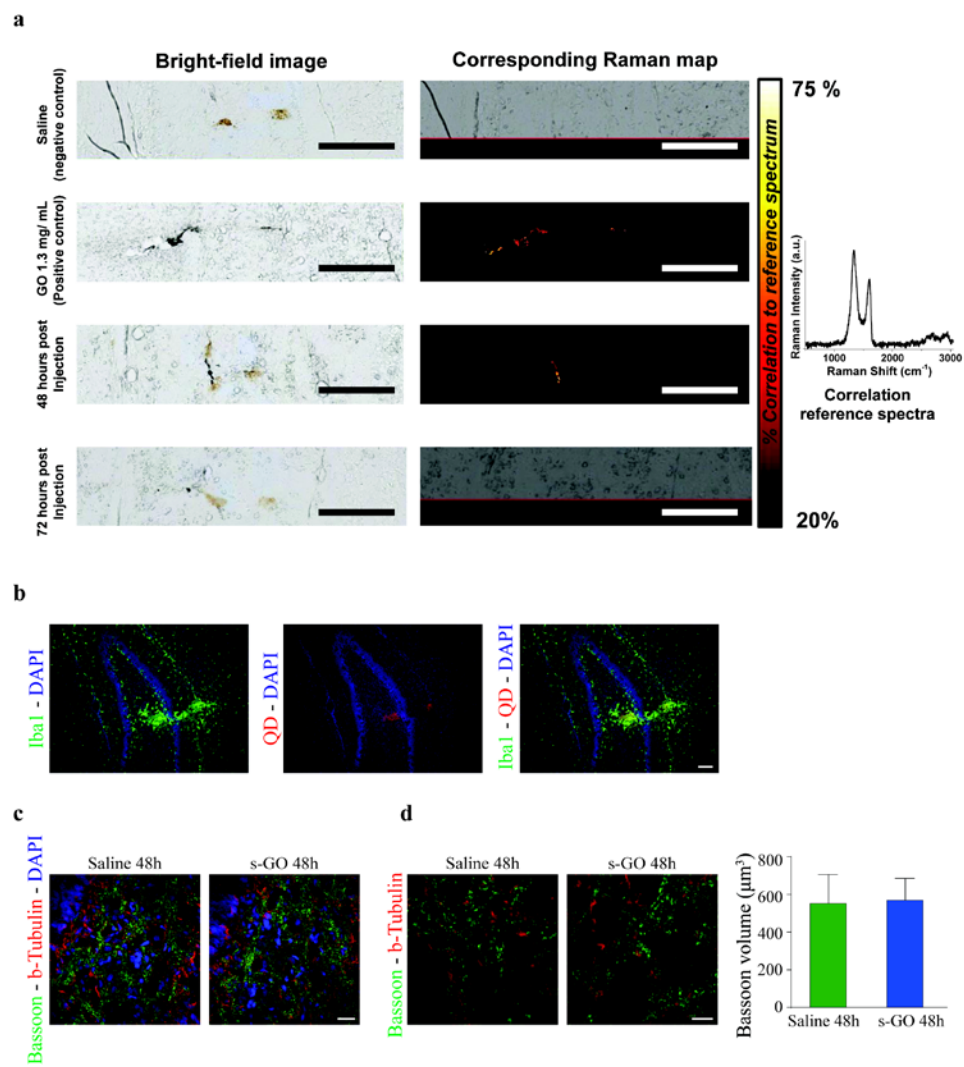


**Figure 4.** In vivo delivery of s-GO is localized and does not alter excitatory synaptic density. In (a) confocal Raman maps were acquired to establish the location of s-GO within cryosectioned dentate gyrus' of s-GO (1.3 mg/mL) treated animals over time (48 h and 72 h). Scale bars = 500 nm. Maps were generated based on the acquired spectra's correlation to a s-GO reference spectra, shown on the right. The dentate gyrus of rats injected with saline (Controls) and rats treated with a higher concentration (1.3 mg/ mL) (positive control) were also examined for comparison. The acquisition parameters were as follows  $\lambda = 633$  nm, laser power = 1 mW, frequency = 25 Hz and a pixel size of 1.6  $\mu\text{m}$ . In (b) Ex vivo fluorescence imaging of hippocampal slices processed for Iba1-positive microglia (in green) and QD linked to s-GO (in red) at the injection site after 48 h. DAPI for nuclei is in blue. Note the precise localization of s-GO within the target area. (c) Ex vivo confocal images of hippocampal synapses at the injection site, excitatory presynaptic terminals were identified by the marker bassoon (in green), in neurons co-labeled with  $\beta$ -tubulin III (in red) and results are shown for saline (control) and s-GO injections after 48 h. DAPI for nuclei is in blue. Analysis has been performed at the higher magnification on  $70 \times 70 \mu\text{m}^2$  ROIs shown in (d) and results are summarized by the bar plots. No differences in bassoon quantification were detected between saline and s-GO injection after 48h. Scale bars: 100  $\mu\text{m}$  in (b), 25  $\mu\text{m}$  in (c) and 10  $\mu\text{m}$  in (d).

608

609 **Figure 5.** Brain tissue reactivity to surgery and s-GO injections after 48 h and 72 h. Ex vivo  
610 hippocampal slices from saline (control) and s-GO injected brains were labeled for GFAP-  
611 positive astrocytes (in green, top row) and Iba1-positive microglia (in red, bottom row) and the  
612 injection site (left dentate gyrus, saline vs. s-GO 50 µg/mL) are shown after 48 h (A) and 72 h  
613 (B). DAPI for nuclei is in blue. Scale bar: 100 µm. Bar plots in (C) and (D) quantify the glial  
614 reaction 48 h and 72 h post- surgery. Comparable values of GFAP and Iba1 immunoreactivity  
615 between saline and s-GO were observed in the hippocampus at 300 µm distance from the  
616 injection site, either lateral or medial in both 48 h and 72 h post-surgery. Notably, at the injection  
617 site, s-GO induced lower GFAP immunoreactivity at 48 h and lower Iba1 immunoreactivity at 72  
618 h when compared to controls. (\*\* P < 0.01 two-way ANOVA).

619

620

621

622



623 ASSOCIATED CONTENT

624 Supplementary Information: Supplementary Figure 1; Supplementary Figure 2

625

626 **Corresponding Author**

627 #E-mail: laura.ballerini@sissa.it

628 #E-mail: kostas.kostarelos@manchester.ac.uk

629 **Author Contributions**

630 R.R. set up the experiments, performed and design electrophysiology and data analysis and  
631 contributed to the writing of the paper; M.M. performed the surgery, histology and confocal  
632 analysis; L.N. performed Raman spectroscopy and S.V. confocal microscopy, while both  
633 contributed to the writing of the results and methods; G.R and A.B. performed the synthesis and  
634 characterization of QD s-GO and contributed to the microscopy; M.P. contributed to the  
635 experimental design; K.K. contributed with synthesis and characterization of GO sheets,  
636 contributed to the experimental design and paper writing; L.B. conceived the idea, the  
637 experimental design and wrote the paper.

638 **Funding Sources**

639 We acknowledged financial support from the European Union's Horizon 2020 research and  
640 innovation program under grant agreements No. 696656 and No. 785219 Graphene Flagship

641

642 **ACKNOWLEDGMENT**

643 We thank E. Aurand for her help in setting the *in vivo* surgeries, A. F. Biagioni for help in  
644 performing histological analysis in vivo, M. Musto and G. Baj for the confocal microscopy at the

Light Microscopy Imaging Center (LMIC) of the University of Trieste-Life Sciences Department and A. F. Rodrigues for synthesis and characterization of GO sheets used in this study. D. Scaini is gratefully acknowledged for useful discussions.

## REFERENCES

- (1) Sanchez, V. C., Jachak, A.R., Hurt, H., Kane, A. B. Biological interactions of graphene-family nanomaterials: an interdisciplinary review. *Chem Res Toxicol.* **2012**, 25, 15-34.
- (2) Kostarelos, K., Novoselov, K. S., Exploring the interface of graphene and biology. *Science.* **2014**, 18, 261-263.
- (3) Mao, H. Y., Laurent, S., Chen, W., Akhavan, O., Imani, M., Ashkarran, A. A., Mahmoudi, M. Graphene: promises, facts, opportunities, and challenges in nanomedicine. *Chem Rev.* **2013**, 8, 3407-3424.
- (4) Novoselov, K. S., et al., Electric field effect in atomically thin carbon films. *Science* **2004**, 306, 666–669.
- (5) Geim, A. K. Graphene: status and prospects. *Science* **2009**, 324, 1530–1534.
- (6) Guo, S., & Dong, S. Graphene nanosheet: synthesis, molecular engineering, thin film, hybrids, and energy and analytical applications. *Chem. Soc. Rev.* **2011**, 40, 2644–2672.
- (7) Novoselov, K. S., et al., Two-dimensional atomic crystals. *Proc. Natl. Acad. Sci. U. S. A.* **2005**, 102, 10451–10453.
- (8) Bitounis, D., Ali-Boucetta, H., Hong, B. H., Min, D. H., Kostarelos, K. Prospects and challenges of graphene in biomedical applications. *Adv. Mater.* **2013**, 25, 2258–2268.
- (9) Kuzum, D., et al., Transparent and flexible low noise graphene electrodes for simultaneous electrophysiology and neuroimaging. *Nat. Commun.* **2014**, 5, 5259.
- (10) Rauti, R., et al., Graphene oxide nanosheets reshape synaptic function in cultured brain networks. *ACS Nano.* **2016**, 10, 4459-71.
- (11) Behar, T. N., et al., Glutamate acting at NMDA receptors stimulates embryonic cortical neuronal migration. *J. Neurosci.* **1999**, 19, 4449-4461.
- (12) Fonnum, F. Glutamate: a neurotransmitter in mammalian brain. *J. Neurochem.* **1984**, 42, 1-11.

- 673 (13) Hirai, K., et al., Inhibiting neuronal migration by blocking NMDA receptors in the  
 674 embryonic rat cerebral cortex: a tissue culture study. *Brain Res. Dev. Brain Res.* **1999**, 114, 63-  
 675 67.
- 676 (14) Palazzo, E., Marabese, I., de Novellis, V., Rossi, F., Maione, S. Supraspinal metabotropic  
 677 glutamate receptors: a target for pain relief and beyond. *Eur J Neurosci.* **2014**, 39, 444-54
- 678 (15) Li, Y., et al., Graphene microsheets enter cells through spontaneous membrane penetration  
 679 at edge asperities and corner sites. *Proc Natl Acad Sci U S A* **2013**, 110, 12295-300
- 680 (16) Mao, J., Guo, R., Yan, L. T. Simulation and analysis of cellular internalization pathways  
 681 and membrane perturbation for graphene nanosheets. *Biomaterials* **2014**, 35, 6069-77
- 682 (17) Rizzoli, S. O. Synaptic vesicle recycling: steps and principles. *EMBO J.* **2014**, 33, 788-822.
- 683 (18) Rodrigues, A. F., et al., A blueprint for the synthesis and characterisation of thin graphene  
 684 oxide with controlled lateral dimensions for biomedicine. *2D Materials* **2018**, 5, 035020
- 685 (19) Tang, X., Ho, W. B., Xue, J. M. Synthesis of Zn-Doped AgInS<sub>2</sub> nanocrystals and their  
 686 fluorescence properties. *J. Phys. Chem. C* **2012**, 116, 9769–9773.
- 687 (20) Adegoke, O., & Forbes, P. B. L-cysteine-capped core/shell/shell quantum dot-graphene  
 688 oxide nanocomposite fluorescence probe for polycyclic aromatic hydrocarbon detection. *Talanta*  
 689 **2016**, 146, 780-788.
- 690 (21) Shang, J., Ma, L., Li, J., Ai, W., Yu, T., Gurzadyan, G. G. The origin of fluorescence from  
 691 graphene oxide. *Sci Rep.* **2012**, 2, 792
- 692 (22) Rao, M. J., Shibata, T., Chattopadhyay, S., Nag, A. Origin of photoluminescence and XAFS  
 693 study of (ZnS)<sub>1-x</sub>(AgInS<sub>2</sub>)<sub>x</sub> nanocrystals. *J Phys Chem Lett.* **2014**, 5, 167-173.
- 694 (23) Li, J., Zhang, Y., Zhang, Z., Tian, Z. Facile synthesis of ZnO Nanorods/GO composite and  
 695 its optical performance. *J Nanosci Nanotechnol.* **2019**, 19, 2379-2384.
- 696 (24) Vempati, S., Celebioglu, A., Uyar, T. Defect related emission versus intersystem crossing:  
 697 blue emitting ZnO/graphene oxide quantum dots. *Nanoscale* **2015**, 7, 16110-16118.
- 698 (25) Raastad, M., Storm, J. F., Andersen, P. Putative single quantum and single fibre excitatory  
 699 postsynaptic currents show similar amplitude range and variability in rat hippocampal slices.  
 700 *Eur. J. Neurosci.* **1992**, 4, 113-117.
- 701 (26) Cellot, G., et al., Carbon nanotube scaffolds tune synaptic strength in cultured neural  
 702 circuits: novel frontiers in nanomaterial-tissue interactions. *J Neurosci.* **2011**, 31, 12945-12953.
- 703 (27) Tyler, E. C., Lovinger, D. M. Metabotropic glutamate receptor modulation of synaptic

- transmission in corticostriatal co-cultures: role of calcium influx. *Neuropharmacology* **1995**, 34, 939-952.
- (28) Malgaroli, A., Tsien, R. W. Glutamate-induced long-term potentiation of the frequency of miniature synaptic currents in cultured hippocampal neurons. *Nature* **1992**, 357, 34-39.
- (29) Richter, K., et al., Gundelfinger, Presynaptic cytomatrix protein bassoon is localized at both excitatory and inhibitory synapses of rat brain. *J Comp Neurol.* **1999**, 408, 437-448.
- (30) Segal, M. Rat hippocampal neurons in culture: responses to electrical and chemical stimuli. *J Neurophysiol* **1983**, 50, 1249-1264.
- (31) Melnick, I. V., Chvanov, M. A., Belan, P. V., Rat hippocampal neurons maintain their own GABAergic synaptic transmission in culture. *Neurosci Lett* **1999**, 262, 151-154
- (32) Galante, M., Nistri, A., Ballerini, L. Opposite changes in synaptic activity of organotypic rat spinal cord cultures after chronic block of AMPA/kainate or glycine and GABAA receptors. *J Physiol.* **2000**, 523, 639-651.
- (33) Gasparini, S., Saviane, C., Voronin, L. L., Cherubini, E. Silent synapses in the developing hippocampus: lack of functional AMPA receptors or low probability of glutamate release? *Proc Natl Acad Sci U S A.* **2000**, 97, 9741-9746
- (34) Rozov, A., Jerecic, J., Sakmann, B., Burnashev, N. AMPA receptor channels with long-lasting desensitization in bipolar interneurons contribute to synaptic depression in a novel feedback circuit in layer 2/3 of rat neocortex. *J Neurosci.* **2001**, 21, 8062-8071
- (35) Murthy, V. N., Sejnowski, T. J., Stevens, C. F. Heterogeneous release properties of visualized individual hippocampal synapses. *Neuron* **1997**, 18, 599-612
- (36) Zucker, R. S. Short-term synaptic plasticity. *Annu Rev Neurosci.* **1989**, 12, 13-31.
- (37) Manabe, T., Wyllie, D. J., Perkel, D. J., Nicoll, R. A. Modulation of synaptic transmission and long-term potentiation: effects on paired pulse facilitation and EPSC variance in the CA1 region of the hippocampus. *J Neurophysiol.* **1993**, 70, 1451-9.
- (38) Debanne, D., Guérineau, N. C., Gähwiler, B. H., Thompson, S. M. Paired-pulse facilitation and depression at unitary synapses in rat hippocampus: quantal fluctuation affects subsequent release. *J Physiol.* **1996**, 491, 163-76.
- (39) Dittman, J. S., & Regehr, W. G. Calcium dependence and recovery kinetics of presynaptic depression at the climbing fiber to Purkinje cell synapse. *J Neurosci.* **1998**, 18, 6147-6162

- (40) Dittman, J. S., Kreitzer, A. C., Regehr, W. G. Interplay between facilitation, depression, and residual calcium at three presynaptic terminals. *J Neurosci.* **2000**, 20, 1374-1385.
- (41) Lana, D., Ugolini, F., Nosi, D., Wenk, G. L., Giovannini, M. G. Alterations in the interplay between neurons, astrocytes and microglia in the rat dentate gyrus in experimental models of neurodegeneration. *Front Aging Neurosci.* **2017**, 9, 296.
- (42) Kawano, H., et al., Role of the lesion scar in the response to damage and repair of the central nervous system. *Cell Tissue Res.* **2012**, 349, 169-180
- (43) Vautrin, J., & Barker, J. L. Presynaptic quantal plasticity: Katz's original hypothesis revisited. *Synapse* **2003**, 47, 184-199
- (44) Kaeser, P. S., & Regehr, W. G. Molecular mechanisms for synchronous, asynchronous, and spontaneous neurotransmitter release. *Annu Rev Physiol.* **2014**, 76, 333-363
- (45) Fioravante, D., & Regehr, W. G. Short-term forms of presynaptic plasticity. *Curr Opin Neurobiol.* **2011**, 21, 269-274
- (46) Li, Y. C., Kavalali, E. T. Synaptic vesicle-recycling machinery components as potential therapeutic targets. *Pharmacol Rev.* **2017**, 69, 141-160
- (47) Bramini, M., et al., Graphene oxide nanosheets disrupt lipid composition, Ca(2+) homeostasis, and synaptic transmission in primary cortical neurons. *ACS Nano* **2016**, 10, 7154-7171
- (48) Sara, Y., Virmani, T., Deák, F., Liu, X., Kavalali, E. T. An isolated pool of vesicles recycles at rest and drives spontaneous neurotransmission. *Neuron* **2005**, 45, 563-573
- (49) Capogna, M. Presynaptic facilitation of synaptic transmission in the hippocampus. *Pharmacol Ther.* **1998**, 77, 203-223
- (50) Rosenmund, C., & Stevens, C. F. Definition of the readily releasable pool of vesicles at hippocampal synapses. *Neuron* **1996**, 16, 1197-1207
- (51) High, B., Cole, A. A., Chen, X., Reese, T. S. Electron microscopic tomography reveals discrete transleft elements at excitatory and inhibitory synapses. *Front Synaptic Neurosci.* **2015**, 7, 9
- (52) Sun, C., et al., Graphene oxide nanosheets stimulate ruffling and shedding of mammalian cell plasma membranes. *Chem.* **2016**, 1, 273-286
- (53) Dante, S., et al., Selective targeting of neurons with inorganic nanoparticles: revealing the crucial role of nanoparticle surface charge. *ACS Nano* **2017**, 11, 6630-6640.

- (54) Zhang, B., Wei, P., Zhou, Z., Wei, T. Interactions of graphene with mammalian cells: molecular mechanisms and biomedical insights. *Adv Drug Deliv Rev.* **2016**, 105, 145-162
- (55) Baldrighi, M., Trusel, M., Tonini, R., Giordani, S. Carbon nanomaterials interfacing with neurons: an in vivo perspective. *Frontiers Neurosci.* **2016**, 10, 250
- (56) Zhou, K., et al., Graphene functionalized scaffolds reduce the inflammatory response and supports endogeneous neuroblast migration when implanted in the adult brain. *Plos One* **2016**, 11, e0151589
- (57) Zhao, F., Zhao, Y., Liu, Y., Chang, X., Chen, C., Zhao, Y. Cellular uptake, intracellular trafficking, and cytotoxicity of nanomaterials. *Small* **2011**, 7, 1322-1337.
- (58) Musto, M., et al., 3D organotypic spinal cultures: exploring neuron and neuroglia responses upon prolonged exposure to graphene oxide. *Front Syst Neurosci.* **2019**, 13, 1.
- (59) Liu, C. W., et al., Graphene-based anticancer nanosystem and its biosafety evaluation using a zebrafish model. *Biomacromolecules* **2013**, 14, 358-366.
- (60) Sydlik, S. A., Jhunjhunwala, S., Webber, M. J., Anderson, D. G., Langer, R. In vivo compatibility of graphene oxide with differing oxidation states. *ACS Nano* **2015**, 9, 3866-3874.
- (61) Mukherjee, S. P., et al., Detection of endotoxin contamination of graphene based materials using the TNF- $\alpha$  expression test and guidelines for endotoxin-free graphene oxide production. *PLoS One* **2016**, 11, e0166816
- (62) Bosi, S., et al., From 2D to 3D: novel nanostructured scaffolds to investigate signalling in reconstructed neuronal networks. *Sci Rep.* **2015**, 5, 9562
- (63) Griguoli, M., Scuri, R., Ragozzino, D., Cherubini, E. Activation of nicotinic acetylcholine receptors enhances a slow calcium-dependent potassium conductance and reduces the firing of stratum oriens interneurons. *Eur J Neurosci.* **2009**, 30, 1011-1022
- (64) Cellot, G., et al., Premature changes in neuronal excitability account for hippocampal network impairment and autistic-like behavior in neonatal BTBR T+tf/j mice. *Sci Rep.* **2017**, 7, 39726
- (65) Tsenov, G., Mátéffyová, A., Mareš, P., Otáhal, J., Kubová, H. Intrahippocampal injection of endothelin-1: a new model of ischemia-induced seizures in immature rats. *Epilepsia* **2007**, 48, 7-13